ARL-TR-9269 ● AUG 2021

DEVCOM ARMY RESEARCH LABORATORY

Analysis of Steady-State Aerodynamic Performance and Control-Surface Effectiveness of a High-Speed Projectile

by Joshua T Bryson

NOTICES

Disclaimers

The findings in this report are not to be construed as an official Department of the Army position unless so designated by other authorized documents.

Citation of manufacturer's or trade names does not constitute an official endorsement or approval of the use thereof.

Destroy this report when it is no longer needed. Do not return it to the originator.

ARL-TR-9269 ● AUG 2021

Analysis of Steady-State Aerodynamic Performance and Control-Surface Effectiveness of a High-Speed Projectile

Joshua T Bryson
Weapons and Materials Research Directorate,
DEVCOM Army Research Laboratory

REPORT DOCUMENTATION PAGE

Form Approved
OMB No. 0704-0188

1. REPORT DATE *(DD-MM-YYYY)*	2. REPORT TYPE	3. DATES COVERED (From - To)
August 2021	Technical Report	1 March–1 July 2021

4. TITLE AND SUBTITLE
Analysis of Steady-State Aerodynamic Performance and Control Surface Effectiveness of a High-Speed Projectile

5a. CONTRACT NUMBER

5b. GRANT NUMBER

5c. PROGRAM ELEMENT NUMBER

6. AUTHOR(S)
Joshua T Bryson

5d. PROJECT NUMBER

5e. TASK NUMBER

5f. WORK UNIT NUMBER

7. PERFORMING ORGANIZATION NAME(S) AND ADDRESS(ES)
DEVCOM Army Research Laboratory
ATTN: FCDD-RLW-WD
Aberdeen Proving Ground, MD 21005

8. PERFORMING ORGANIZATION REPORT NUMBER
ARL-TR-9269

9. SPONSORING/MONITORING AGENCY NAME(S) AND ADDRESS(ES)

10. SPONSOR/MONITOR'S ACRONYM(S)

11. SPONSOR/MONITOR'S REPORT NUMBER(S)

12. DISTRIBUTION/AVAILABILITY STATEMENT
Approved for public release: distribution unlimited.

13. SUPPLEMENTARY NOTES
ORCID ID: Joshua Bryson, 0000-0002-0753-6823

14. ABSTRACT

A methodology is presented to analyze the performance characteristics of a marginally stable projectile with the goal to improve maneuverability while minimizing drag and achieving reasonable control surface/deflection requirements. This approach is illustrated with an example guided projectile and used to analyze the flight dynamics across the intended flight envelope to evaluate the maneuverability/stability properties and the flight-control and actuator system requirements. The maneuverability is assessed through a series of analyses of the trimmed conditions to show the angle of attack and deflection required to achieve optimal lift-to-drag ratio across flight conditions. The longitudinal stability derivative and short-period dynamics are presented to evaluate the stability properties across the flight envelope.

15. SUBJECT TERMS
flight dynamics, aerodynamics, maneuverability analysis, lift-to-drag, stability, guided projectile

16. SECURITY CLASSIFICATION OF:			17. LIMITATION OF ABSTRACT	18. NUMBER OF PAGES	19a. NAME OF RESPONSIBLE PERSON
a. REPORT	b. ABSTRACT	c. THIS PAGE			Joshua T Bryson
Unclassified	Unclassified	Unclassified	UU	28	19b. TELEPHONE NUMBER (Include area code) (410) 306-1939

Contents

List of Figures

List of Tables

Acknowledgments

Special thanks to Dr Joseph D Vasile of DEVCOM Army Research Laboratory, and Dr Ashish Nedungadi of The Johns Hopkins University Applied Physics Laboratory, for their help and discussions regarding the analysis, modeling, and presentation of the projectile aerodynamics. Special thanks to Clayton Smith of Sandia National Laboratories for his input regarding the flight dynamics analysis and presentation of results.

1. Introduction

Improving the maneuverability of guided projectiles enables range extension using gliding maneuvers, and terminal-phase maneuverability enables the projectile to engage imperfectly located targets and evade active protection systems.[1–3] Additionally, operating at higher velocities is advantageous for many military projectile applications, particularly in the terminal phase of flight but across the entire trajectory as well. Projectiles lacking an in-flight propulsion system rely on low-drag designs to preserve as much of the launch energy as possible. Thus, the maneuverability and drag characteristics are important to consider for projectile design.

The aerodynamics determined by the airframe and control-surface design are among the main drivers of maneuverability and drag for guided projectiles, including the overall lift capability, the baseline drag, and the careful coordination of the center of pressure and center of gravity (CG) to achieve marginal stability across the flight envelope. A marginally stabile design enables the projectile to be oriented to a desired angle of attack (AoA) to generate lift while using minimal control deflection to minimize drag effects.

Current research into low-drag, high-lift airframes for both supersonic and subsonic flight regimes is improving the understanding of desirable features of the airframe design while reducing design-cycle iteration time to rapidly evolve capabilities.[4] One approach to long-range projectile design leverages a symmetric flight body with low-aspect-ratio fins for stability, lift, and control. For these designs, the static forces and moments can vary substantially with aerodynamic roll angle at moderate to high AoAs desired for most maneuvers.[5–6]

This research presents an approach to analyze the characteristics and flight dynamics of a guided projectile across the intended flight envelope to evaluate the maneuverability/stability properties and the lift, drag, and lift-to-drag (L/D) ratio. This methodology is illustrated on a gun-launched guided projectile but is applicable to missile-/rocket-propelled systems as well. The projectile design is presented briefly, and the aerodynamic model is summarized. The steady-state trim analysis methodology is outlined, and the analysis on stability and lift-to-drag is presented, followed by an analysis of the control-surface effectiveness. Finally, an analysis of the short-period dynamics is presented to inform flight-control and actuation-system requirements.

2. Airframe Description

The Laboratory Technology Vehicle (LTV) is an engineering test-bed projectile used by the US Army Combat Capabilities Development Command Army Research Laboratory to experiment with various gun-launched, guided flight and maneuver technologies. The LTV flight body was shaped through a series of optimization analyses that identified design candidates with low drag and high L/D ratios while maintaining marginal stability across the supersonic Mach regime.[4–6] The body is 105 mm in diameter and 10 cal (1.05 m) in length with a 0.5-cal 7° boattail, and has a CG located 6.0 cal back from the nose. The projectile has a 30% ogive nose as a trade-off between drag and payload volume. There are four low-aspect-ratio fins arrayed symmetrically around the body. The projectile is designed to be sabot launched from an 8-inch-diameter gun with no deploying aerodynamic surfaces, which limits the fin span to 8 inches tip to tip. Figure 1 shows an illustration of the LTV flight body in a configuration with a 10.5-mm-radius rounded nose tip and 80-mm-chord control surfaces hinged at their leading edges. The mass properties for this variant are given in Table 1.

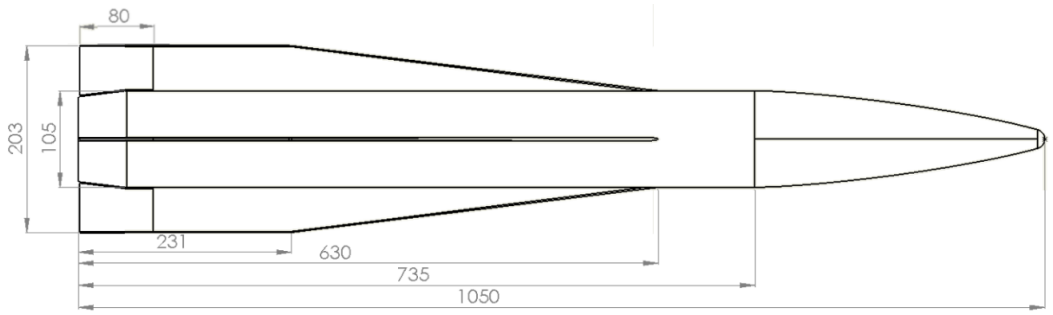

Fig. 1 LTV flight body with rounded nose and 80-mm control surfaces hinged at the leading edge. Dimensions given in millimeters.

Table 1 Mass properties for LTV

Mass properties	
Mass	16.8 kg
CG_X	588 mm (56%) from nose
CG_Y, CG_Z	On center line
I_{XX}	0.0273 kg-m^2
I_{YY}, I_{ZZ}	1.247 kg-m^2

For this analysis, the projectile is configured to fly in the "X" configuration with the roll angle location of movable surface i given by $\phi_{MAS}^{i} = [45°, 135°, 225°, 315°]$ for $\delta_1, \delta_2, \delta_3, \delta_4$, respectively, as illustrated in Fig. 2.

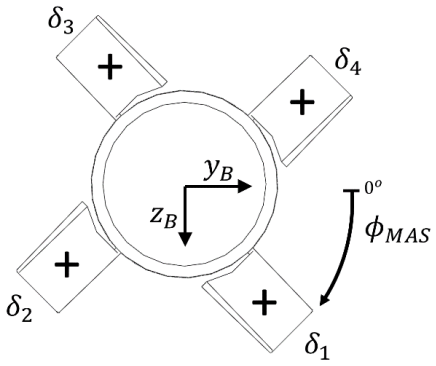

Fig. 2 Numbering scheme of the movable aerodynamic surfaces along with the deflection sign convention. View is from projectile base.

The control mixing of the four movable surfaces into virtual control channels is given in Eqs. 1–3:

$$\delta_p = \frac{1}{4}(-\delta_1 - \delta_2 - \delta_3 - \delta_4) \tag{1}$$

$$\delta_q = \frac{1}{4}(-\delta_1 + \delta_2 + \delta_3 - \delta_4) \tag{2}$$

$$\delta_r = \frac{1}{4}(-\delta_1 - \delta_2 + \delta_3 + \delta_4) \tag{3}$$

3. Aerodynamic Model

The aerodynamic model uses coefficients based on Mach and AoA to provide the aerodynamic forces and moments.[7–9] Aerodynamic data describing the forces and moments due to the fin-tab control surfaces, termed movable aerodynamic surfaces (MAS), is calculated and applied separately from the aerodynamic data for the assembly of the body and fixed fin surfaces, referred to as fixed aerodynamic surfaces (FAS).

The FAS aerodynamic component model given in Eqs. 4–9 contains the aerodynamic forces and moments from the FAS in the nonrolling aerodynamic coordinate frame (Fig. 3), with each coefficient dependent on Mach number and aerodynamic roll angle.

$$F_X = -QS\left[C_{A_0}(M,\phi_A) + C_{A_{\bar{\alpha}^2}}(M,\phi_A)\sin^2\bar{\alpha} + C_{A_{\bar{\alpha}^4}}(M,\phi_A)\sin^4\bar{\alpha}\right] \tag{4}$$

$$F_Y = QS[C_{S_0}(M,\phi_A) + C_{S_{\bar{\alpha}}}(M,\phi_A)\sin\bar{\alpha} + C_{S_{\bar{\alpha}^2}}(M,\phi_A)\sin^2\bar{\alpha} + C_{S_{\bar{\alpha}^3}}(M,\phi_A)\sin^3\bar{\alpha} + C_{S_{\bar{\alpha}^4}}(M,\phi_A)\sin^4\bar{\alpha} + C_{S_{\bar{\alpha}^5}}(M,\phi_A)\sin^5\bar{\alpha}] \tag{5}$$

$$F_Z = -QS\left[C_{N_0}(M,\phi_A) + C_{N_{\bar{\alpha}}}(M,\phi_A)\sin\bar{\alpha} + C_{N_{\bar{\alpha}^2}}(M,\phi_A)\sin^2\bar{\alpha} + C_{N_{\bar{\alpha}^3}}(M,\phi_A)\sin^3\bar{\alpha} + C_{N_{\bar{\alpha}^4}}(M,\phi_A)\sin^4\bar{\alpha} + C_{N_{\bar{\alpha}^5}}(M,\phi_A)\sin^5\bar{\alpha}\right] \quad (6)$$

$$M_L = QSD[C_{l_0}(M,\phi_A) + C_{l_{\bar{\alpha}}}(M,\phi_A)\sin\bar{\alpha} + C_{l_{\bar{\alpha}^2}}(M,\phi_A)\sin^2\bar{\alpha} + C_{l_p}(M,\phi_A)\frac{pD}{2V}] \quad (7)$$

$$M_M = QSD\left[C_{m_0}(M,\phi_A) + C_{m_{\bar{\alpha}}}(M,\phi_A)\sin\bar{\alpha} + C_{m_{\bar{\alpha}^2}}(M,\phi_A)\sin^2\bar{\alpha} + C_{m_{\bar{\alpha}^3}}(M,\phi_A)\sin^3\bar{\alpha} + C_{m_{\bar{\alpha}^4}}(M,\phi_A)\sin^4\bar{\alpha} + C_{m_{\bar{\alpha}^5}}(M,\phi_A)\sin^5\bar{\alpha} + \tilde{C}_{m_q}(M,\phi_A)\frac{qD}{2V}\right] \quad (8)$$

$$M_N = QSD\left[C_{n_0}(M,\phi_A) + C_{n_{\bar{\alpha}}}(M,\phi_A)\sin\bar{\alpha} + C_{n_{\bar{\alpha}^2}}(M,\phi_A)\sin^2\bar{\alpha} + C_{n_{\bar{\alpha}^3}}(M,\phi_A)\sin^3\bar{\alpha} + C_{n_{\bar{\alpha}^4}}(M,\phi_A)\sin^4\bar{\alpha} + C_{n_{\bar{\alpha}^5}}(M,\phi_A)\sin^5\bar{\alpha} + \tilde{C}_{n_r}(M,\phi_A)\frac{rD}{2V}\right] \quad (9)$$

where α is the body AoA, β is the body angle of sideslip, $\bar{\alpha} = \sqrt{\alpha^2 + \beta^2}$ is the total body AoA, D is the projectile diameter, V is the projectile velocity, $Q = \frac{1}{2}\rho V^2$ is the dynamic pressure, and $S = \frac{\pi}{4}D^2$ is the aerodynamic reference area. The $\widetilde{C}_{m_q}$ and $\widetilde{C}_{n_r}$ are the pitch and yaw damping sums, which include both the C_{m_q} and C_{n_r} terms as well as the angular rate terms $C_{m_{\dot{\alpha}}}$ and $C_{n_{\dot{\beta}}}$.

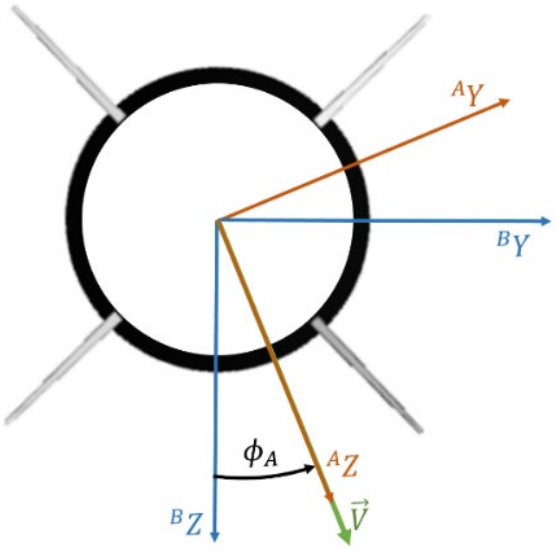

Fig. 3 The nonrolling aerodynamic coordinate system and body-fixed coordinate system for the projectile. View is from projectile base, with both X axes into the page. The coordinate systems are related through a ϕ_A rotation about X, with the ^{B}Y, ^{B}Z projection of the projectile translational velocity vector, $\vec{V}$, aligned to the ^{A}Z axis.

The MAS aerodynamic model is similar in form and sums the force and moment contributions of the four movable fin-flap surfaces arrayed around the body in the nonrolling aerodynamic coordinate frame. For the full details on the MAS aerodynamic model, see Bryson et al.[9]

4. Steady-State Trim-Analysis Methodology

An analysis of the aerodynamic forces and moments is conducted across the flight envelope by exercising the aerodynamic model with the ranges of Mach, altitude, aerodynamic roll angle, body AoA, and control-surface deflection angle. Conditions where the moments, C_l, C_m, C_n, are all zero correspond to steady-state trim conditions, which are of particular interest in evaluating the flight performance of a projectile design. As previously discussed, the critical metrics for this application are the maneuverability (i.e., lift capability) and drag, but also important are controllability metrics such as stability and control effectiveness.

At each flight condition, [Mach, Alt], the set of control deflections, $[\delta_p\ \delta_q\ \delta_r]$, are identified, which balances the total aerodynamic moments to zero for each $\bar{\alpha}, \phi_A$ pair. The aerodynamic forces and moments are calculated at these trim conditions for each point within the flight envelope and are used to analyze the maneuverability and controllability metrics of interest. Figure 4 illustrates this process for standard-day sea level (SSL), Mach 2, for an example of $\bar{\alpha} = 5^o$, $\phi_A = 0^o$ (in the body pitch plane). The C_m for the projectile with undeflected control surfaces is shown as a solid blue line, which is shifted through increasing δ_q deflection angle until the $C_m = 0$ trim point reaches $\bar{\alpha} = 5^o$, shown with a dotted blue line. Following this process for $[\delta_p\ \delta_q\ \delta_r]$ simultaneously, the trim conditions for the projectile are identified across the flight envelope for use in subsequent analyses.

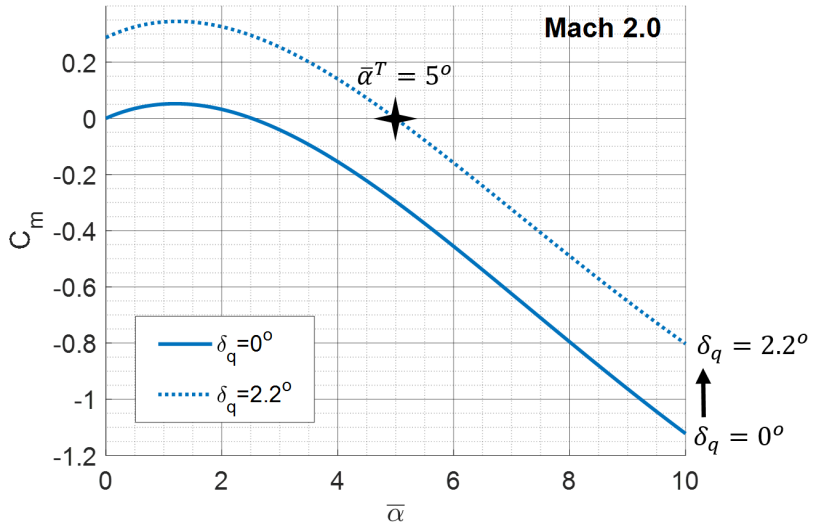

Fig. 4 Illustration of trimming procedure for $\bar{\alpha}^T = 5^o$ at Mach 2, $\phi_A = 0^o$, SSL. C_m is plotted for varying $\bar{\alpha}$ for showing the undeflected case ($\delta_q = 0^o$) along with $\delta_q = 2.2^o$ corresponding to the $C_m = 0^o$ trim condition at $\bar{\alpha}^T = 5^o$ shown with the black star.

As a measure of maneuverability balanced with controllability, the stability derivatives of the projectile at these trim conditions are analyzed across the flight envelope. The design goal for this projectile is to achieve marginal stability across the supersonic flight regime while minimizing the unstable regions within the subsonic–supersonic flight envelope. Figure 5 plots the longitudinal stability derivative, $\frac{\partial C_m}{\partial \bar{\alpha}}$, at trim conditions for varying $\bar{\alpha}, \phi_A$ at Mach 0.8, 2, 3, and 4 at SSL. The analysis shows the projectile exhibits a small unstable region at small α across Mach, surrounded by marginally stable conditions moving to more stable as α increases.

The aerodynamic properties for this projectile are known to be ϕ_A-dependent,[5–6] and this is well illustrated in Fig. 5. The stability properties are symmetric in ϕ_A every 90^o, and less stable regions correspond to $\bar{\alpha}$'s oriented along $\phi_A = [0^o, \pm 90^o, \pm 180^o, \dots]$. The remainder of the analysis presented in this research will focus on pitch plane maneuvers in the "X" flight orientation ($\phi_A = 0^o$) for simplicity, but these methodologies can be trivially extended to analyze maneuverability across ϕ_A.

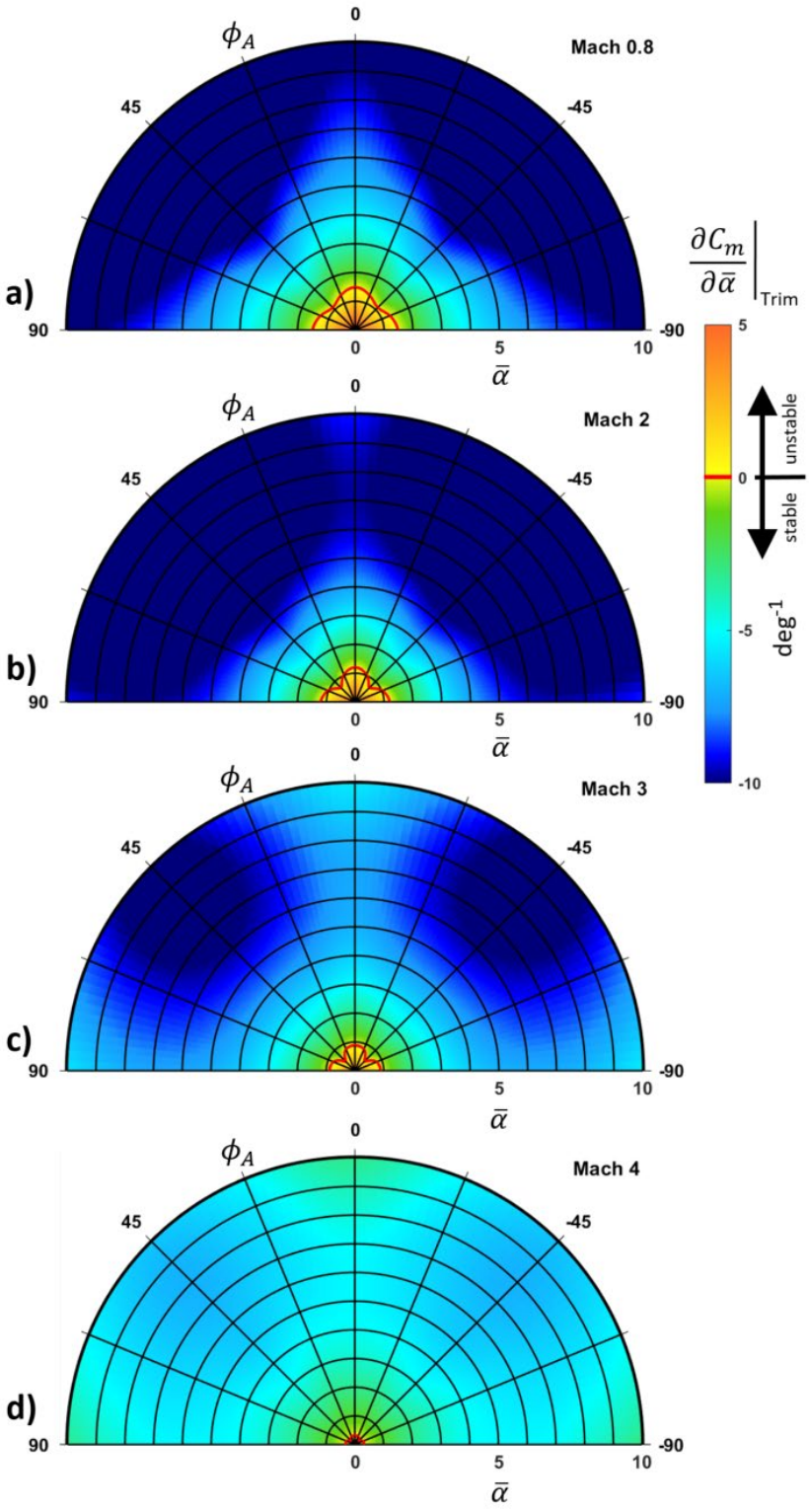

Fig. 5 Longitudinal stability derivative values for the projectile at trim for Mach 0.8, 2, 3, and 4 at sea level. The projectile is unstable at small $\bar{\alpha}$, and has varying stability properties across ϕ_A, with symmetry every 90^o.

5. Maneuverability Analysis: L/D, Load Factor

The projectile maneuverability is assessed by analyzing the L/D and the load factor to determine the lateral acceleration capabilities and evaluate the extent to which the flight speed could be eroded by drag forces during a sustained maneuver. Following the previously presented trim methodology, the total forces at trim are identified across the Mach, Altitude flight envelope and used to obtain total lift force, L, and drag force, D.

At each [Mach, Alt, ϕ_A] condition, there is value of $\bar{\alpha}^T$ that maximizes the L/D of the projectile. Operating at or near this optimal L/D condition results in a compromise between maximizing lift and maneuverability while minimizing drag to maintain flight velocity.

Figure 6 shows an analysis of trim conditions and resulting L/D for Mach 0.8, 2, and 3 at SSL. Figure 6a, c, and e plot C_m, C_N across $\bar{\alpha}, \delta_q$, with dashed lines indicating constant $\bar{\alpha}$ countours and solid lines representing constant δ_q contours. Points along the $C_m = 0$ line are valid steady-state trim conditions, which generate the corresponding C_N value at each $\bar{\alpha}, \delta_q$ configuration. Figure 6b, d, and f plot L/D at trim across $\bar{\alpha}^T$, with the maximum L/D trim condition marked with red squares on each figure.

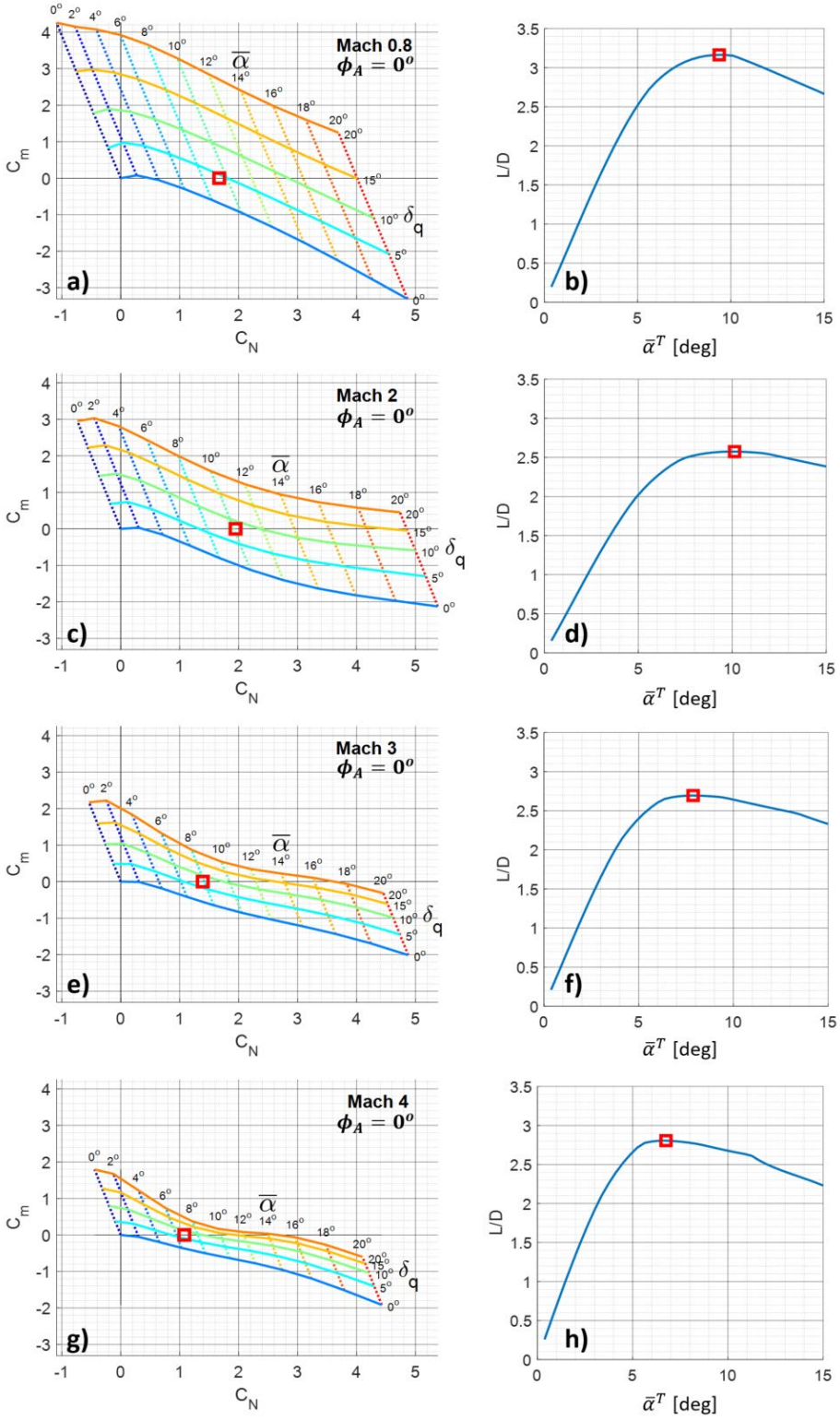

Fig. 6 Analysis at flight condition: sea level, $\phi_A = 0^o$ for Mach 0.8, 2, 3, and 4. Subfigures a), c), e), and g) show pitch plane stability data: C_N and C_m for varying $\bar{\alpha}, \delta_q$. Subfigures b), d), f), and h) show L/D at trim ($C_m = 0$) across $\bar{\alpha}$. The points of maximum L/D for each Mach number are shown as red squares.

Figure 7 presents the L/D at trim for flight across Mach at sea level. Figure 7a plots the maximum L/D at trim, which is generally near 2.5 for supersonic flight and around 3 for high-subsonic flight. Figure 7b and c plot L/D at trim across $\bar{\alpha}^T$ and Mach. Along with the particular maximum L/D, the shape of the L/D curve in Figure 7b is of interest in the maneuverability assessment, with a broad region of near-maximum L/D desirable for operational flexibility. Figure 7 shows the location and value of the upper and lower $\bar{\alpha}^T$ boundaries region with at least 90% of the max L/D to provide a better representation of the available region for near-optimal maneuver. In the regions where the 90% max L/D point lies outside the flight envelope of $\bar{\alpha} \leq 15^o$, it is clipped to 15^o for this analysis.

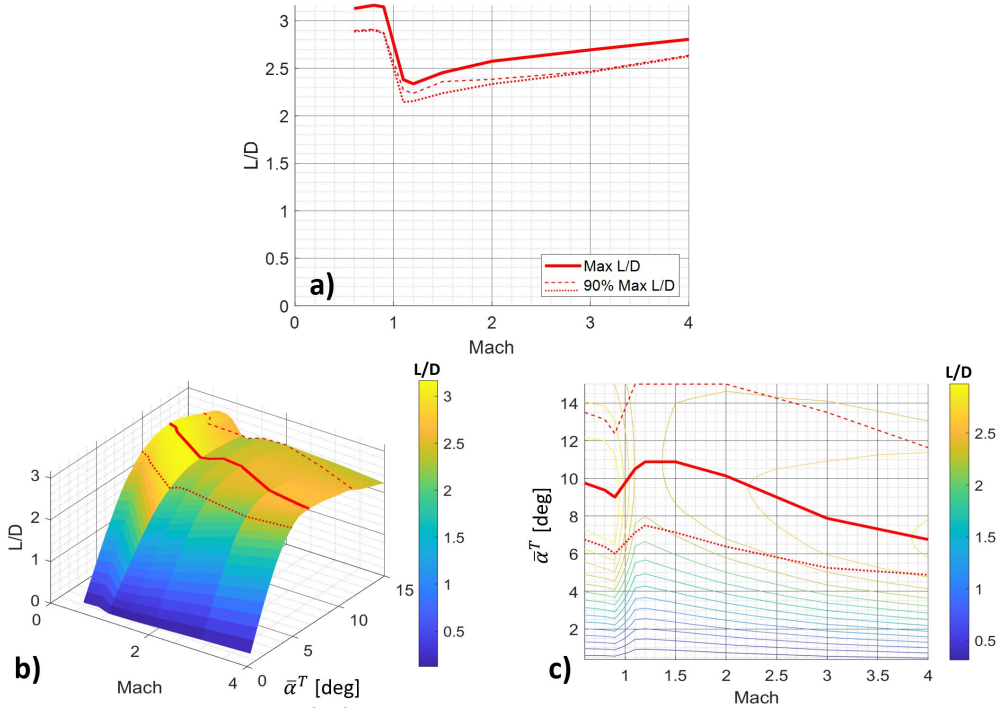

Fig. 7 L/D at trim conditions across Mach at sea level, $\phi_A = 0^o$. Maximum L/D at trim across Mach is plotted in a), along with the 90% max L/D values. b) and c) show surface and contour plots, respectively, of trim L/D across the Mach and $\bar{\alpha}^T$. The values of $\bar{\alpha}^T$ corresponding to maximized L/D at each Mach are shown as a solid red line, with 90% max L/D region boundaries shown in dashed/dotted red.

An analysis of the load factor experienced by the projectile can be helpful for understanding of L/D values across the maneuver envelope in a more intuitive form. The load factor calculations used in this analysis calculate the specific acceleration (force/mass) associated with L and D forces and normalizes that value by the acceleration of gravity, as shown in Eqs. 10 and 11.

$$D_{LF} = \left(\frac{D}{mg}\right) \tag{10}$$

$$L_{LF} = \left(\frac{L}{mg}\right) \tag{11}$$

These load factors express the projectile accelerations in multiples of the gravitational acceleration, and are unit-less quantities but typically expressed in g's. Figure 8 plots the load factors across Mach experienced at the maximum L/D trimmed flight conditions and at the 90% max L/D conditions. These results are highly dependent on dynamic pressure but show a general capability to achieve lateral accelerations in excess of 40 g's with acceptable drag throughout Mach 2–4 at SSL. The dashed and dotted lines in Fig. 8 show the upper and lower $\bar{\alpha}^T$ bounds corresponding to 90% of the max L/D flight condition, respectively, to provide a representation of the available region for near-optimal maneuver.

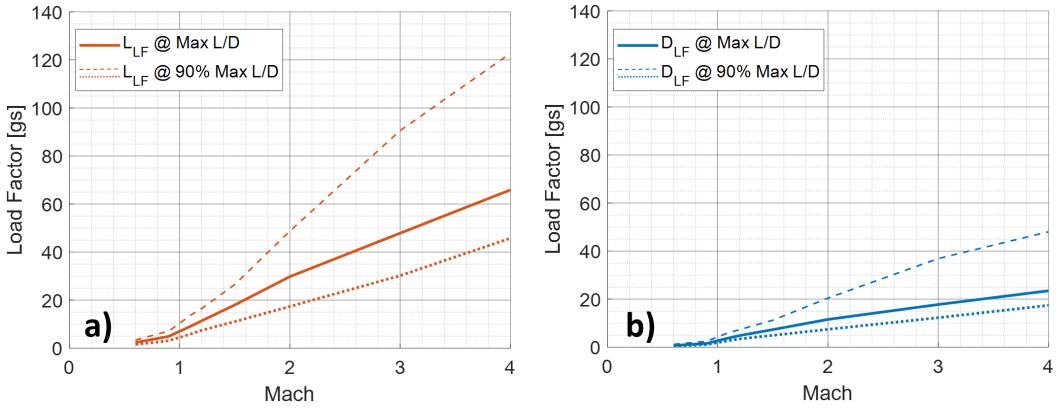

Fig. 8 Load factors associated with L and D at trim across Mach for $\phi_A = 0^o$, SSL

6. Control Effectiveness Analysis

In addition to the maneuverability, the overall control-effectiveness and control-deflection requirements at trim are important factors to analyze. Control deflection angles that are too high can have issues with flow separation and loss of effectiveness, indicate the control surfaces are undersized, and/or indicate the CG location should be adjusted to decrease the projectile stability. Figure 9 shows the virtual pitch-control deflection, δ_q^T, required to trim maximum L/D and 90% maximum L/D across Mach at sea level along with the associated $\bar{\alpha}^T$ for comparison. Values corresponding to maximum L/D and 90% max L/D shown in solid and dashed red lines, respectively. The results show control-deflection requirements between $5^o - 8^o$ are generally required to trim at maximum L/D across the flight envelope, indicating an acceptable combination of control-surface sizing and CG placement.

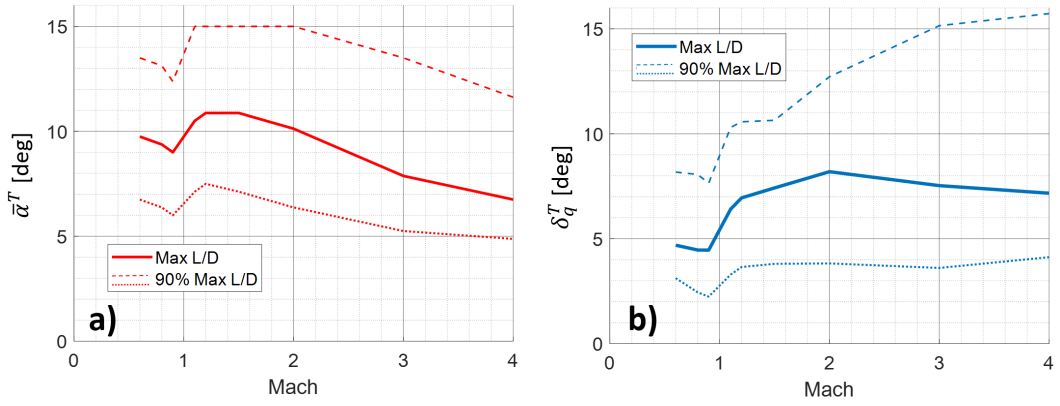

Fig. 9 AoA, $\bar{\alpha}^T$, and pitch-control deflection, δ_q^T, for flight at trim condition across Mach for sea level, $\phi_A = 0^o$. Values required for trim at maximum L/D are plotted with solid lines, and values for trim at 90%, boundaries of maximum L/D are plotted with dashed and dotted lines.

Another factor of interest relating to control effectiveness is the ratio between $\bar{\alpha}^T$ and δ_q^T, hereafter referred to as the α/δ ratio. The design goal for this projectile is $1 < \alpha/\delta < 2$. At lower α/δ, the control surfaces would begin to stall and lose effectiveness before desired α is achieved, and larger deflection angles often require higher torque/power from the actuator systems. At higher α/δ, the projectile is extremely responsive to slight changes or noise in the deflection angle, and the actuator may struggle with the precision required to accurately position the control surfaces. Figure 10 plots α/δ at trim for maximum L/D and 90% maximum L/D across Mach, showing the α/δ value generally stays above 1 except for near Mach 4 and stays below 2 for all supersonic flight. Figure 11 summarizes the relations between $\bar{\alpha}^T$, δ_q^T, and the load factor achieved by the projectile at various Mach numbers.

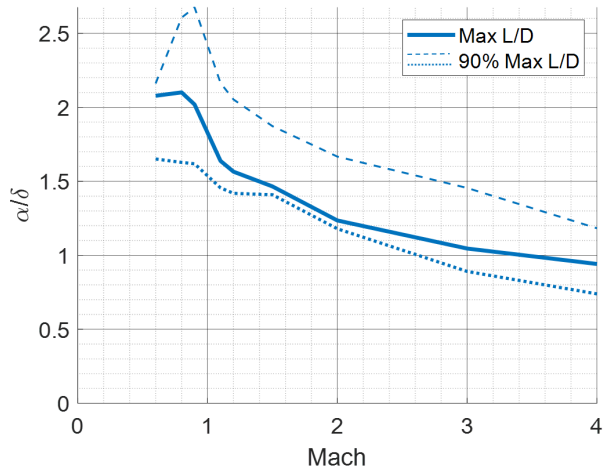

Fig. 10 Ratio of α/δ at trim condition for maximum L/D and 90% maximum L/D across Mach for sea level, $\phi_A = 0^o$

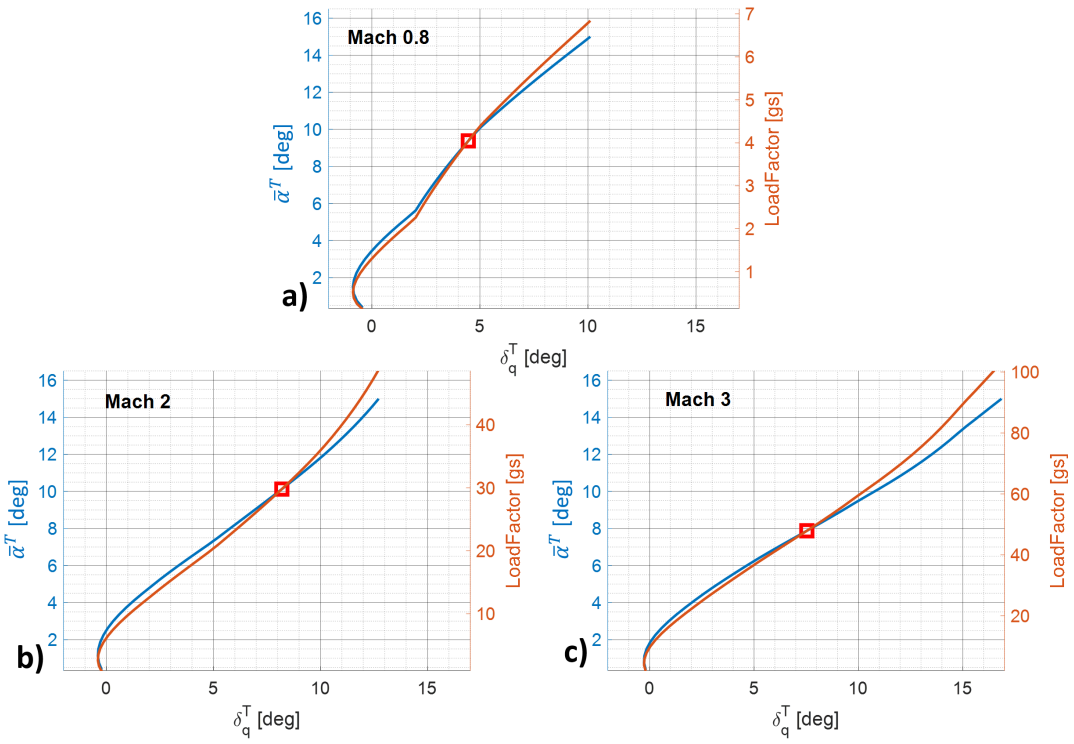

Fig. 11 Control effectiveness plots summarizing the relations among $\bar{\alpha}^T$, δ_q, and the load factor achieved by the projectile at various Mach numbers, SSL. The point of maximum L/D is shown as a red square on each plot for reference.

7. Short-Period Dynamics Analysis

The short-period mode of the projectile longitudinal dynamics is also analyzed to help evaluate the maneuverability and to inform the flight-control and actuator design requirements. Due to the projectile symmetry, this analysis of the behavior/motion in the pure pitch plane represents the yaw-plane dynamics as well. However, the aerodynamic asymmetry of the projectile with ϕ_A requires an evaluation of the short-period mode along both $\phi_A = 0^o$, and 45^o, or equivalently, for the longitudinal plane of the projectile in both the "x" and "+" flight orientations. Figure 5 and Bryson et al.[9] show the projectile to be generally more stable at $\phi_A = 45^o$, which will increase the natural frequency in that orientation. These higher frequencies are important to consider when determining overall flight control and actuator requirements.

The short period natural frequency and damping ratio, $\omega_{n_{SP}}$ and ζ_{SP}, are approximated using Eqs. 12 and 13, respectively[10,11]:

$$\omega_{n_{SP}} \approx \sqrt{\frac{Z_\alpha M_q}{u_0} - M_\alpha} \tag{12}$$

$$\zeta_{sp} \approx -\frac{\left(M_q + M_{\dot{\alpha}} + \frac{Z_\alpha}{u_0}\right)}{2\omega_{n_{SP}}} \tag{13}$$

where u_0 is the projectile velocity and the longitudinal derivative terms $Z_\alpha, M_\alpha, M_q,$ and $M_{\dot{\alpha}}$ are defined in Eqs. 14–17:

$$Z_\alpha = -\frac{QS}{m}\left(C_{L_\alpha} + C_{D_0}\right) \tag{14}$$

$$M_\alpha = \frac{QSD}{I_y}\, C_{m_\alpha} \tag{15}$$

$$M_q = \frac{QSD}{I_y}\frac{D}{2u_0} C_{m_q} \tag{16}$$

$$M_{\dot{\alpha}} = \frac{QSD}{I_y}\frac{D}{2u_0} C_{m_{\dot{\alpha}}} \tag{17}$$

As previously noted, the aerodynamic model for this projectile does not break out the individual contributions of C_{m_q} and $C_{m_{\dot{\alpha}}}$, but rather has the damping terms included only as a combined sum. For the calculation of ζ_{SP}, these terms are used together as a sum so the available data can be used without complication. For the $\omega_{n_{SP}}$ calculation, $C_{m_{\dot{\alpha}}}$ is assumed to be 1/3 of C_{m_q} to estimate C_{m_q} from the total damping sum, $\tilde{C}_{m_q}$.[10] For this projectile, the $\frac{Z_\alpha M_q}{u_0}$ term containing this C_{m_q} estimate in the $\omega_{n_{SP}}$ approximation is small relative to the M_α term, so errors introduced by this assumption are minor.

The longitudinal derivatives, Eqs. 14–16, are evaluated locally at each trim condition and used to calculate $\omega_{n_{SP}}$ and ζ_{SP} across the projectile flight envelope. Figures 12 and 13 plot the $\omega_{n_{SP}}$ and ζ_{SP} across $\bar{\alpha}^T$, Mach for $\phi_A = 0^o$ and 45^o, respectively. As expected from Eq. 12, $\omega_{n_{SP}}$ increases with dynamic pressure and spans a large range across the Mach numbers within the flight envelope. The damping ratio remains small across the flight envelope. The approximation for the damping ratio calculation assumes positive damping and is not valid in regions where the projectile is unstable, so the unstable portions of the flight envelope are left off the plots.

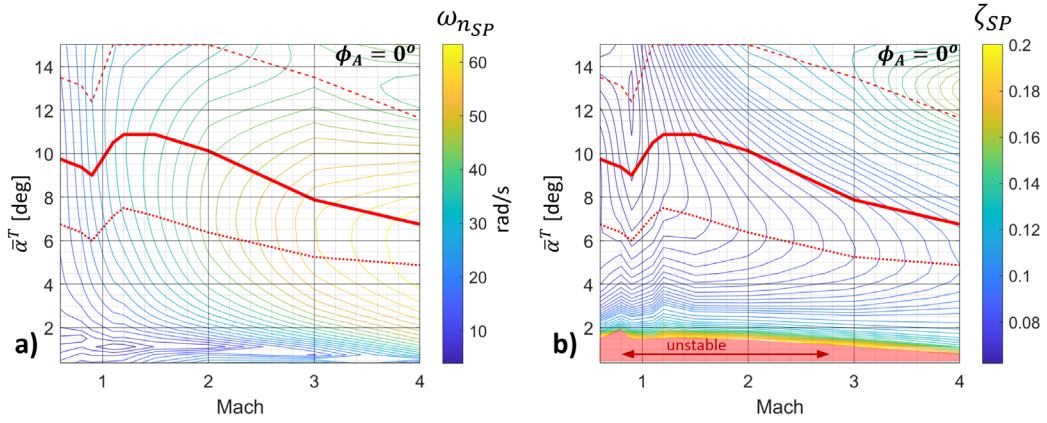

Fig. 12 Plots of $\omega_{n_{SP}}$ and ζ_{SP} across $\bar{\alpha}^T$, Mach for $\phi_A = 0^o$, SSL. Flight conditions corresponding to maximum L/D and 90% maximum L/D are shown in solid and dotted red lines, respectively.

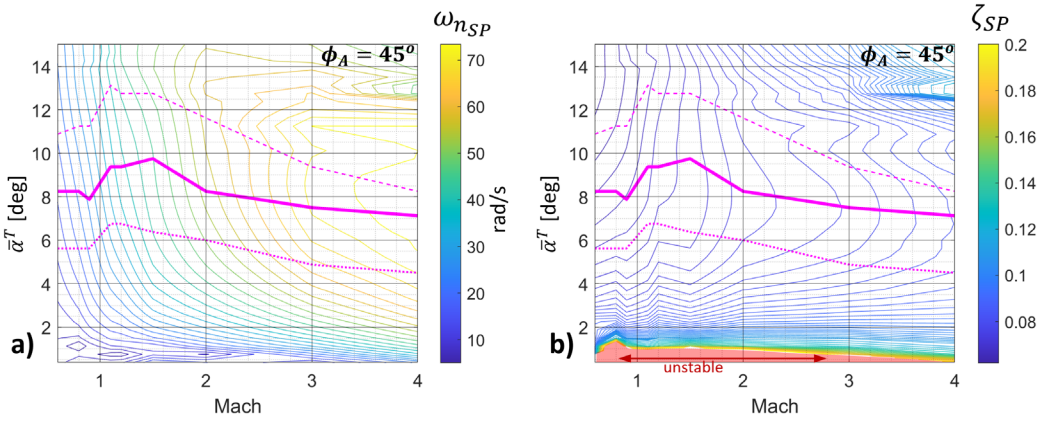

Fig. 13 Plots of $\omega_{n_{SP}}$ and ζ_{SP} across $\bar{\alpha}^T$, Mach for $\phi_A = 45^o$, SSL. Flight conditions corresponding to maximum L/D and 90% maximum L/D for $\phi_A = 45^o$ are shown in solid and dotted pink lines, respectively.

The roots of the characteristic equation for the short period approximation are calculated as

$$\lambda_{1,2} = -\zeta_{sp}\omega_{n_{SP}} \pm i\omega_{n_{sp}}\sqrt{1-\zeta_{sp}^2} \tag{18}$$

Using the values of $\omega_{n_{SP}}$ and ζ_{SP} at $\phi_A = 0^o$ and 45^o, the short period poles are calculated for the maximum L/D and 90% maximum L/D flight conditions across Mach, and plotted together in Fig 14. The poles for the lower speed conditions begin near the origin and move out to higher frequencies as Mach increases. Lines of constant Mach are plotted as solid, while lines of constant $\bar{\alpha}^T$ are dotted. Lines indicating the maximum L/D condition for varying Mach at SSL are also shown in each plot as red for $\phi_A = 0^o$ and pink for $\phi_A = 45^o$, following Figs. 12 and 13, respectively.

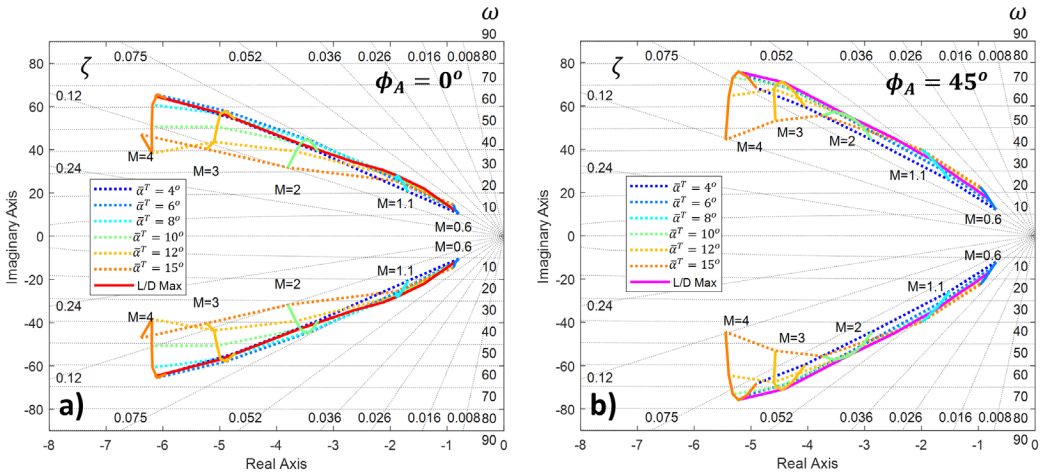

Fig. 14 Map of the short period poles for the projectile across $\bar{\alpha}^T$ and Mach for $\phi_A = 0^o, 45^o$. Lines of constant Mach are solid, while lines of constant $\bar{\alpha}^T$ are dotted. Lines indicating the maximum L/D condition for varying Mach at SSL are also shown in each plot.

8. Conclusion

A methodology was presented to analyze the performance characteristics of a marginally stable projectile with the goal to evaluate overall maneuverability while minimizing drag and determining whether control-surface deflection requirements are reasonable. This approach was illustrated with a gun-launched guided projectile and used to analyze the maneuverability and flight dynamics across the intended flight envelope. The trimmed flight conditions were identified and used to find the maximum L/D operating points across the flight envelope. An analysis of the longitudinal stability, load factor, and control effectiveness was presented to explore the maneuverability/stability properties. Finally, an analysis of the short-period dynamics was presented to further evaluate the maneuverability/stability characteristics and to inform the flight-control and actuator requirements development.

9. References

1. Costello M. Extended range of a gun launched smart projectile using controllable canards. Shock Vibration. 2001;8:203–213.
2. Fresconi FE. Range extension of gun-launched smart munitions. Presented at International Ballistics Symposium; 2008.
3. Bryson JT, Vasile JD, Celmins I, Fresconi FE. Approach for understanding range extension of gliding indirect fire munitions. AIAA Scitech. 2018;3158.
4. Vasile JD, Bryson JT, Fresconi FE. Aerodynamic design optimization of long range projectile using missile DATCOM. AIAA Scitech. 2020:1762.
5. Vasile J, Sahu J. Roll orientation-dependent aerodynamics of a long-range projectile. DEVCOM Army Research Laboratory (US); 2020 Aug. Report No.: ARL-TR-9017.
6. Vasile J, Bryson J, Sahu J, Paul J, Gruenwald B. Aerodynamic dataset generation of a long-range projectile. DEVCOM Army Research Laboratory (US); 2020 Aug. Report No.: ARL-TR-9019.
7. McCoy RL. Modern exterior ballistics. Schiffer; 2012.
8. Zipfel PH. Modeling and simulation of aerospace vehicle dynamics. AIAA Education Series; 2007 Apr. https://arc.aiaa.org/doi/book/10.2514/4.862182.
9. Bryson J, Vasile J, Gruenwald B, Saju J, Fresconi F. Modeling and flight dynamics of a projectile with nonlinear, roll-dependent aerodynamics. AIAA Scitech. 2021:0823.
10. Nelson RC. Flight stability and automatic control. 2nd ed. WCB/McGraw Hill; 1998.
11. Yechout TR Morris SL, Bossert DE, Hallgren WF, Hall JK. Introduction to aircraft flight mechanics. 2nd ed. AIAA Education Series; 2014 Jan.

Nomenclature

α	=	body angle of attack in pitch plane
$\bar{\alpha}$	=	total body angle of attack, $\sqrt{\alpha^2 + \beta^2}$
$\bar{\alpha}^T$	=	total body angle of attack at steady-state trim condition
β	=	body angle of sideslip in yaw plane
$C_{A_0}, C_{A_{\bar{\alpha}^2}}, C_{A_{\bar{\alpha}^4}}$	=	zeroth, second and fourth order axial force coefficient
$C_{l_0}, C_{l_{\bar{\alpha}}}, C_{l_{\bar{\alpha}^2}}$	=	zeroth, first and second order roll moment coefficient
C_{L_α}	=	lift coefficient derivative with respect to α
C_{l_p}	=	roll damping coefficient
$C_{N_0}, C_{N_{\bar{\alpha}}}, C_{N_{\bar{\alpha}^i}}$	=	zeroth, first and ith order fit coefficients for normal force
C_m	=	coefficient of pitching moment
$C_{m_0}, C_{m_{\bar{\alpha}}}, C_{m_{\bar{\alpha}^i}}$	=	zeroth, first and ith order fit coefficients for static pitch moment
C_{m_q}	=	pitch damping coefficient
$C_{n_0}, C_{n_{\bar{\alpha}}}, C_{n_{\bar{\alpha}^i}}$	=	zeroth, first and ith order fit coefficients for static yaw moment
C_{n_r}	=	yaw damping coefficient
$C_{S_0}, C_{S_{\bar{\alpha}}}, C_{S_{\bar{\alpha}^i}}$	=	zeroth, first and ith order fit coefficients for side force
D	=	reference diameter
p	=	roll rate
ϕ_A	=	aerodynamic roll angle
q	=	pitch rate
Q	=	½ ρV2 , dynamic pressure
r	=	yaw rate
S	=	D2π/4, aerodynamic reference area

List of Symbols, Abbreviations, and Acronyms

Alt	altitude
AoA	angle of attack
CG	center of gravity
FAS	fixed aerodynamic surfaces
L/D	lift-to-drag
LTV	Laboratory Technology Vehicle
MAS	movable aerodynamic surfaces
SSL	standard-day sea level

1 (PDF) DEFENSE TECHNICAL INFORMATION CTR DTIC OCA

1 (PDF) DEVCOM ARL FCDD RLD DCI TECH LIB

18 (PDF) DEVCOM ARL FCDD RLW A F E FRESCONI FCDD RLW W T SHEPPARD FCDD RLW WD L STROHM J BRYSON B BURCHETT I CELMINS B C GRUENWALD J DESPIRITO L FAIRFAX J PAUL J D VASILE FCDD RLW WA N TRIVEDI FCDD RLW WB J SADLER FCDD RLW WC M MINNICINO FCDD RLW WE M ILG B TOPPER D EVERSON FCDD RLW WF E RIGAS